Materials Science & Engineering A 770 (2020) 138548

Contents lists available at ScienceDirect

Materials Science & Engineering A

journal homepage: http://www.elsevier.com/locate/msea

Eutectic phase strengthening and strain rate sensitivity behavior of AZ80 magnesium alloy

Lingbao Ren [a,c], Mingyang Zhou [b], Tianhui Lu [b], Lingling Fan [b], Yangyang Guo [b], Yuwenxi Zhang [b], Carl J. Boehlert [d,**], Gaofeng Quan [b,*]

[a] Shaanxi Key Laboratory of Low Metamorphic Coal Clean Utilization, School of Chemistry and Chemical Engineering, Yulin University, Yulin, 719000, PR China
[b] School of Materials Science and Engineering, Southwest Jiaotong University, Chengdu, 610031, PR China
[c] Center for Advancing Materials Performance from the Nanoscale, State Key Laboratory for Mechanical Behavior of Materials, Xi'an Jiaotong University, Xi'an, 710049, PR China
[d] Department of Chemical Engineering and Materials Science, Michigan State University, East Lansing, MI, 48824, USA

ARTICLE INFO

Keywords:
Magnesium
High strength
Eutectic phase
Strain rate sensitivity

ABSTRACT

A Mg–8Al-0.5Zn-0.2Mn wt.% (AZ80) alloy, containing a high volume percent of the β eutectic phase, was prepared using extrusion without a homogenization pretreatment (EX-II(F)). The β-eutectic-phase contributions to grain refinement, texture tailoring, and plastic behavior were discussed. Microstructure characterization was presented along with a strengthening mechanism analysis. The β-eutectic-phase strengthening contributions to the yield strength were estimated according to the thermal mismatch, Orowan looping, load transfer, and Hall-Petch mechanisms. In addition, the temperature and strain dependence for strain rate sensitivity (SRS) were investigated, and the influence of aging on the SRS evolution was discussed. The SRS exponent, m, of the EX-II(F) was measured at 298–573 K using strain rate jumps between 10^{-4} s^{-1}-10^{-3} s^{-1}. The m-value increased with increasing strain and temperature, and decreased with grain coarsening and Al solute depletion. Aging precipitation exhibited a softening effect on the 473–573 K flow stress and resulted in higher m-values. The β eutectic phase cracking decreased with increasing test temperature, which was attributed to the high deformability of the β eutectic phase above 573 K. Overall, this work has shown that the β eutectic phase can serve as a means to strengthen extruded AZ80.

1. Introduction

The β-$Mg_{17}Al_{12}$ intermetallic compound, which forms both during solidification (β eutectic phase) and aging processes (β precipitate) [1,2], has a body-centered cubic structure (bcc, $a = 1.05$ nm) [3] and exhibits a higher density ($\rho = 2.09$ g/cm^3) and Young's modulus ($E = 72$–78 GPa) than the α-Mg matrix ($\rho = 1.74$ g/cm^3, $E = 45$ GPa) [4]. It also exhibits a lower elongation-to-failure (ε_f) than the α-Mg matrix at room temperature (RT) [5], and the β precipitates has a primary habit plane parallel to the basal plane of the α-Mg matrix [2]. The number of β precipitate per unit volume after 473 K aging is at least an order of magnitude less than that in high-strength Al alloys [6]. The β eutectic phase, which forms during the solidification in as-cast Mg–Al alloys [7], can serve as in situ reinforced particles, and its strengthening effect has yet to be studied in wrought Mg alloys after thermomechanical treatment. Recently, Zha et al. [8] showed that a microstructure containing a high volume percent of β particles, which formed along the grain boundaries at elevated temperatures, resulted in high superplasticity for rolled AZ91. Taking advantage of the β eutectic phase may introduce a new strengthening path for conventional Mg alloys such as extruded AZ80.

The plastic behavior of Mg alloys is strongly related to the strain rate sensitivity (SRS) [9]. The SRS exponent was extracted from the power law model of plastic deformation, which has often been used to evaluate the effect of strain rate on the flow stress as:

$$\sigma = C\dot{\varepsilon}^m \tag{1}$$

where m is the SRS exponent, σ is the flow stress, $\dot{\varepsilon}$ is the strain rate. The m-value can be calculated as:

* Corresponding author.
** Corresponding author.
E-mail addresses: boehlert@egr.msu.edu (C.J. Boehlert), quangf@swjtu.edu.cn (G. Quan).

https://doi.org/10.1016/j.msea.2019.138548
Received 12 March 2019; Received in revised form 18 September 2019; Accepted 12 October 2019
Available online 14 October 2019

Table 1
The processing conditions for the AZ80 alloys.

Conditions	Post-casting heat treatments
As-cast	None
EX-I(F)	693 K/8 h homogenization prior to extrusion, extruded at 573 K and 0.5 mm/s
EX-II(F)	No homogenization prior to extrusion, extruded at 573 K and 0.5 mm/s
EX-II(T5)	443 K/15 h aging treatment after EX-II(F)

$$m = \partial(\ln(\sigma) / \partial(\ln(\dot{\varepsilon})) \quad (2)$$

The m-value is an intrinsic material parameter which governs the rate-dependent mechanical properties [10]. High SRS is always associated with a greater resistance to neck development. SRS is significantly affected by both the deformation conditions (temperature, strain rate, and imposed strain) and microstructural features (grain size, twin density, and solute concentration). Severe grain refinement results in enhancement of the m-values due to changes in the deformation mechanisms [11,12]. For example, 2 μm-ultrafine-grained Mg-2Gd wt.% alloys exhibited $m = 0.47$ at 673 K [13], which facilitated superplastic deformation and grain boundary sliding (GBS) [14]. The decreased SRS observed with increasing Al solute concentration is likely due to dynamic strain aging from the interaction between the Al solute and dislocations [15]. Moreover, a negative SRS was observed in AZ31 when more tension twinning was activated with increasing strain rates [16, 17].

The m-value is also related to the apparent activation volume (V_{app}) for plastic deformation:

$$V_{app} = \sqrt{3}kT \Big/ (m \cdot \sigma) \quad (3)$$

where k is the Boltzmann constant (1.380649×10^{-23} J/K) and T is the absolute temperature. A higher m-value leads to a smaller V_{app}. The V_{app} is the rate of decrease of the activation enthalpy with respect to flow stress at a fixed temperature [18] and can be directly related to the deformation mechanisms [9,19].

In this study, AZ80, containing a high volume percent of the β eutectic phase, was prepared using extrusion without a homogenization pretreatment. The β-eutectic-phase contributions to grain refinement, texture tailoring, and plastic behavior were discussed. Microstructure characterization was presented along with a strengthening mechanism analysis. In addition, the temperature dependence and strain dependence for SRS were investigated, and the influence of aging on the SRS evolution was discussed.

2. Materials and experimental procedure

As-cast AZ80 alloys were prepared by resistance melting targeted amounts of pure Mg (99.9 wt%), pure Al (99.9 wt%), pure Zn (99.9 wt %), and a Mg–10Mn (wt.%) master alloy. The molten Mg was protected by a covering flux and CO_2+2 vol% SF_6 mixed gas. The melt was held at 1013 K for 50–60 min, then poured into a 95 mm diameter steel die, which was preheated at 523 K. The cast billet was then machined to an 88 mm diameter. The parameters of the post-casting heat treatments are listed in Table 1. Two different extrusion methods, EX-I(F) and EX-II(F), were used to tailor the extruded microstructure, where "F" represents no post-extrusion treatments. For the EX-I(F), the billets were homogenized at 693 K for 8 h prior to extrusion. For the EX-II(F), the billet was quickly heated using electromagnetic induction for about 10–15 min until its temperature reached 573 K prior to extrusion. The pre-heated temperature in EX-II(F) was far below the melting temperature of the β eutectic phase ($T_{m(\beta)} = 710$ K). Thus, most of the β eutectic phase was retained during the extrusion process [1]. Both extrusions were carried out at 573 K with a ram speed of 0.5 mm/s followed by air cooling to produce 16 mm diameter round bars. A 443 K/15 h aging treatment (T5) was performed after the EX-II(F) extrusion, which was termed as EX-II(T5).

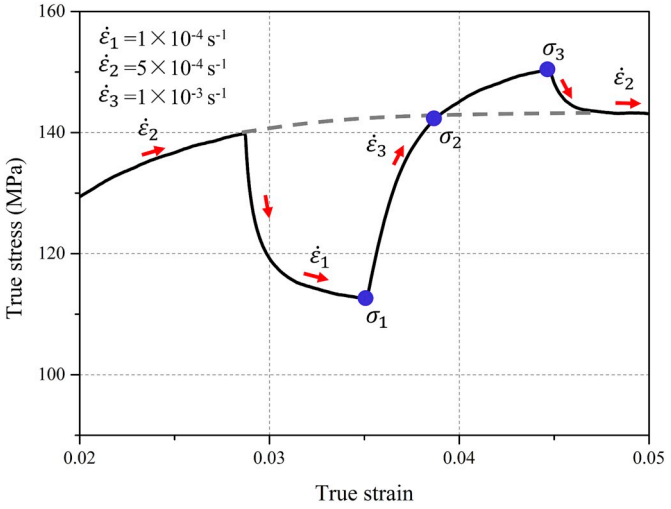

Fig. 1. Schematic of a representative strain rate jump (SRJ) at $\varepsilon = 3\%$.

Tensile specimens, with a 5 mm gage diameter and 30 mm gage length, were electro-discharge machined along the extrusion direction (ED). Uniaxial tension tests were carried out at RT using a MTS-CMT5105 universal testing machine. A constant crosshead displacement rate (1.8 mm/min), corresponding to an initial strain rate of 10^{-3} s^{-1}, was maintained during the uniaxial tension tests. Strain rate jump (SRJ) tests were performed at 298 K, 373 K, 473 K, and 573 K at strain rates of 10^{-4} s^{-1} ($\dot{\varepsilon}_1$), 5×10^{-4} s^{-1} ($\dot{\varepsilon}_2$), and 10^{-3} s^{-1} ($\dot{\varepsilon}_3$). The test temperatures were maintained within ±1 K using a furnace equipped with three chromel–alumel thermocouples. Prior to the SRJ test, the specimen was kept for 5 min at the target temperature which is necessary to guarantee the center temperature of the AZ80 tensile bar reaches the target temperature. During the test, a base strain rate of ($\dot{\varepsilon}_2$) was adopted, and the cyclic strain rate jumps ($\dot{\varepsilon}_2 \rightarrow \dot{\varepsilon}_1 \rightarrow \dot{\varepsilon}_3 \rightarrow \dot{\varepsilon}_2$) were repeated four times at strain levels of $\varepsilon = 3\%$, 6%, 9%, 12%. A schematic of a SRJ at $\varepsilon = 3\%$ is shown in Fig. 1. The strain rate started from the base strain rate $\dot{\varepsilon}_2$, and the strain rate was then decreased to $\dot{\varepsilon}_1$ at the true stress of σ_1, and then increased to $\dot{\varepsilon}_3$ at the true stress of σ_3. The true stress σ_2 was obtained at $\dot{\varepsilon}_2$. As a result, the m-value at $\varepsilon = 3\%$ was measured based on the variation of true stresses (σ_1, σ_2, σ_3) with strain rates ($\dot{\varepsilon}_1$, $\dot{\varepsilon}_2$, $\dot{\varepsilon}_3$) according to Equ. (2).

The microstructure of the as-processed and tested alloys was observed using a ZEISS A1 optical microscope (OM) and a TESCAN MIRA III FEG scanning electron microscope (SEM) equipped with an EDAX-TSL energy dispersive spectroscopy (EDS) system. The average grain sizes and volume percents of the secondary phases were estimated by the line intercept method (GB/T 6394–2017) and the grid point method (GB/T 228.1–2010), respectively [20]. Electron back-scattered diffraction (EBSD) was performed on the ED plane of the round bars, and the post-processing was performed using EDAX OIM Analysis 7 software. The SEM accelerating voltage was 30 kV, and the working distance was 16 mm. Metallographic samples were sequentially ground using silicon carbide (SiC) papers through 800, 1200, 2400, and 4000 grits, respectively. They were then polished through 1.0 μm and 0.25 μm diamond paste, and 0.04 μm colloidal silica solution was used for the final mechanical polishing. The samples for OM and SEM observation were etched using a solution containing 60 ml ethanol, 20 ml water, 15 ml acetic acid, and 5 ml nitric acid. The phases were identified using a Panalytical X'Pert Pro X-ray diffraction (XRD) system with Cu $K_{\alpha 1}$ radiation ($\lambda = 0.154$ nm), and the selected XRD parameters were 30 kV, 50 mA at 293 K with 2θ values ranging between 20-90°. The foil samples for transmission electron microscopy (TEM, Tecnai G2 F20) observation were produced by ion milling with a precision ion polishing system (PIPS, Gatan 691), and the phases were identified by selected area electron diffraction (SAED) in the TEM.

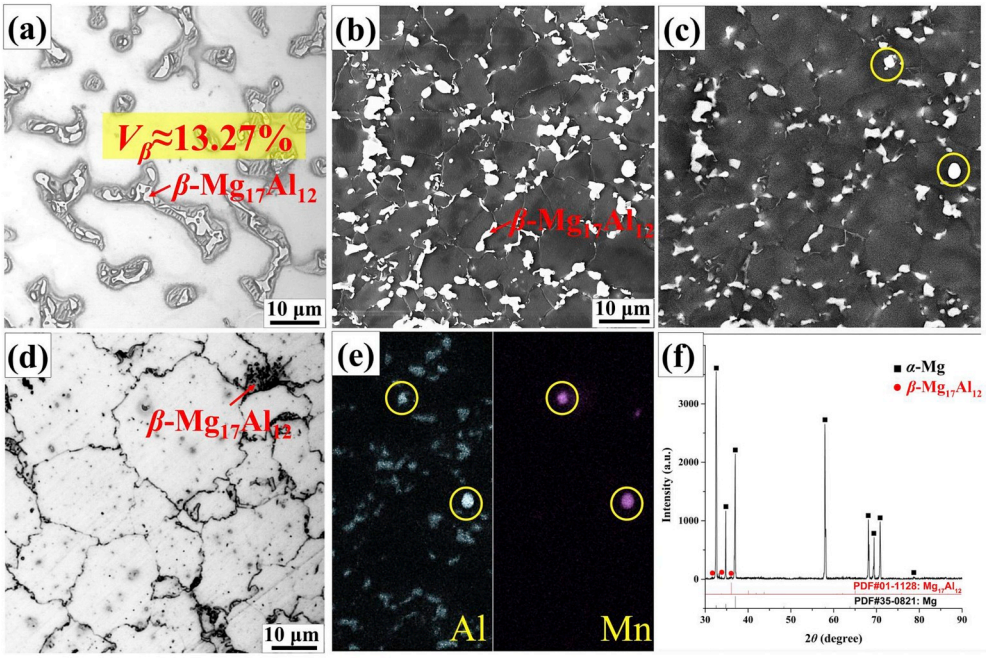

Fig. 2. (a) Optical photomicrograph of the as-cast AZ80 microstructure; (b) SE-SEM image and (c) BSE-SEM image for the EX-II (F) in the ED plane; (d) Optical photomicrograph of the EX-I(F) in the ED plane; (e) EDS map illustrating the Al and Mn distribution for EX-II(F). The highlighted yellow circles are consistent with the locations circled in (c); (f) X-ray diffraction (XRD) pattern for the EX-II(F). (For interpretation of the references to colour in this figure legend, the reader is referred to the Web version of this article.)

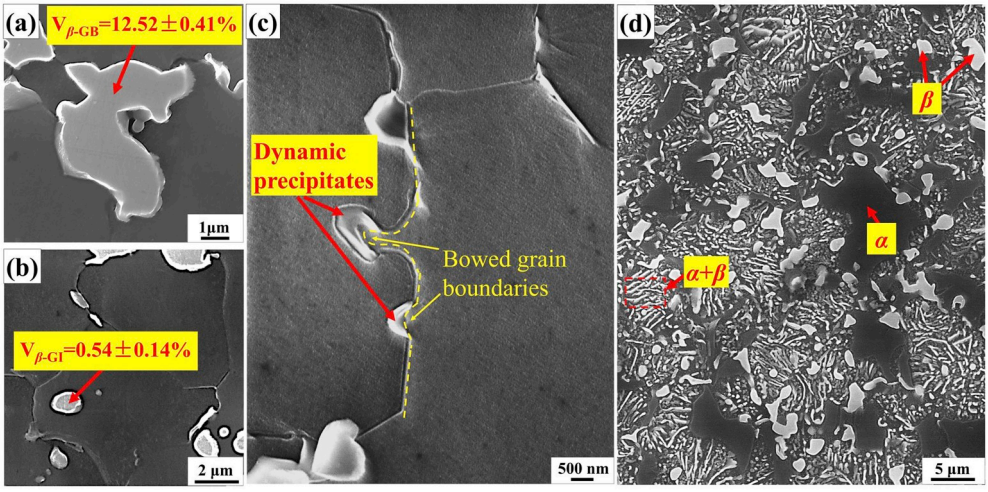

Fig. 3. (a) and (b) SE-SEM photomicrographs of the β eutectic phase in the grain boundary (β-GB) and grain interior (β-GI), respectively, in EX-II(F); (c) SE-SEM photomicrographs of the grain boundaries precipitates in the EX-II(F); (d) SE-SEM photomicrograph of EX-II(T5) microstructure.

3. Results and discussion

3.1. AZ80 microstructure in different processing conditions

The microstructure of the as-cast AZ80 was composed of the α-Mg matrix and approximately 13 vol% β eutectic phase [1] (Fig. 2 (a) and (d)) shows the microstructure of the EX-I(F) in the ED plane. No β eutectic phase was retained in the extruded microstructure, which indicated that most of the eutectic was dissolved in the matrix after the 693 K/8 h homogenization treatment. The average α-Mg grain size was 26 μm, and a small volume percent of discontinuous β precipitates (DPs) formed near the grain boundaries. Fig. 2 (b, c) show the secondary electron (SE) and backscattered electron (BSE) SEM images, respectively, of the EX-II(F) microstructure (in the ED plane), which exhibited a 10 μm average α-Mg grain size; the 1–3 μm diameter granular particle phases were evenly distributed both on the grain boundary (GB) and in the grain interior (GI) of the matrix. Based on the EDS map (Fig. 2 (e)), the Al-rich granular phase was prevalent in EX-II(F), and there were a small volume percent of Al–Mn particles (highlighted in yellow circles). The XRD pattern (Fig. 2 (f)) clarified that there were mainly α-Mg and β-$Mg_{17}Al_{12}$ phases present in the EX-II(F). Thus, most of the granular Mg–Al phase in EX-II(F) was assumed to be the β eutectic phase.

The volume percents of the β eutectic phase in the GB and GI were 12% and 0.5%, respectively, which is consistent with the initial amount of the β eutectic phase in the as-cast AZ80 (Fig. 3(a, b)) . This suggests that most of the β eutectic phase was retained in EX-II(F). Dynamic precipitation occurred on the bowed GBs (Fig. 3 (c)). Tan et al. [21] reported that dynamic precipitates near the bowed GBs could relax the stress concentration and suppress grain growth during dynamic recrystallization (DRX). Fig. 3 (d) presents the microstructure of EX-II(T5). The β eutectic phase accounted for 12 vol% of the microstructure, which was similar to the amount of β eutectic phase present before aging. This indicated that the β eutectic phase was stable during the 443 K/15 h aging process. An additional 28 vol% of lamellar DPs formed after aging.

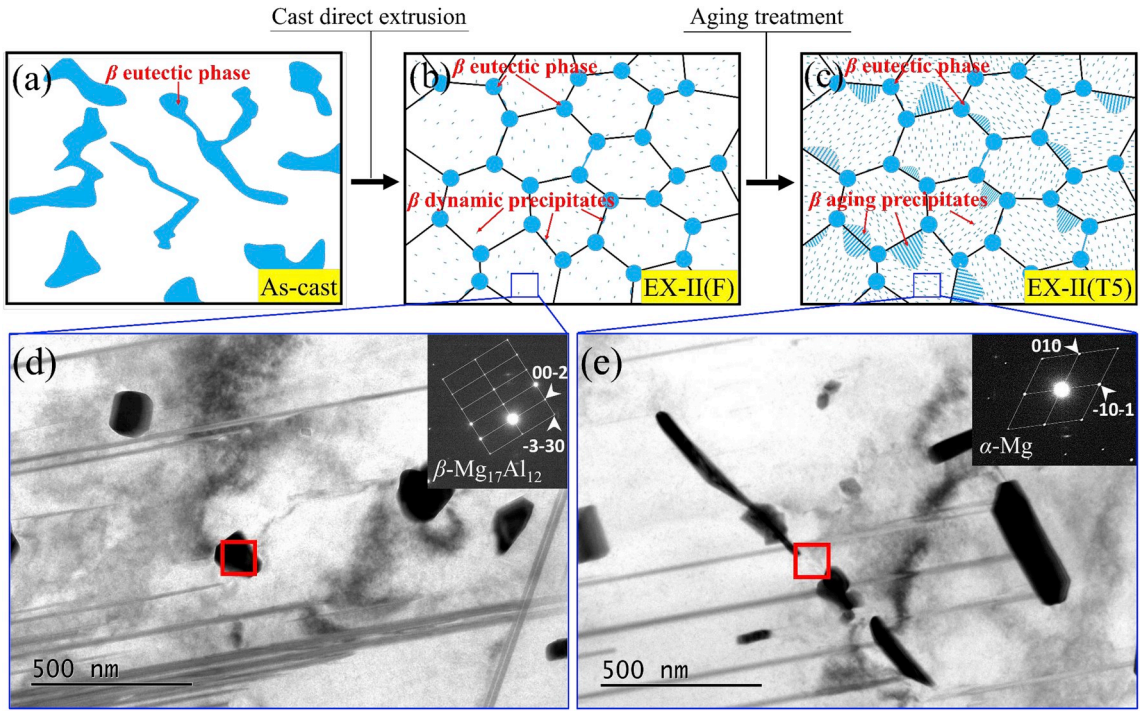

Fig. 4. Schematic maps for the secondary phase evolution in different processing conditions. (a) as-cast; (b) EX-II(F); (c) EX-II(T5); (d) and (e) are the TEM images for the β precipitates in the EX-II(F) and EX-II(T5), respectively.

According to the equilibrium Mg–Al binary phase diagram, Mg–8Al wt. % should have a maximum β volume percent of about 13% at 443 K [9]. However, the EX-II(T5) contained three times that amount. Barbagallo et al. [1] found that the composition of the β eutectic particles was 37 wt % Al, which was lower than the 42 wt% Al equilibrium concentration according to the Mg–Al phase diagram. Recently, Mørtsell et al. [22] reported a precipitate stacking configuration, β_2'', containing vacated columns in its unit cell, that required less solute to create the same volume percent of the precipitates. This may help explain the larger-than-expected β volume in the EX-II(T5). The schematic map of the evolution of the secondary phases during the cast-direct-extrusion and subsequent aging process are shown in Fig. 4. The β eutectic phase was fragmented into the fine β particles during the extrusion and most of them distributed near the GBs, see Fig. 3 (a, b). In addition, the dynamic β precipitation occurred in the as-extruded alloy. Fig. 4 (b, d) illustrate the dynamic precipitation in the GBs and α-matrix which was confirmed by the TEM results. The continuous/discontinuous precipitation density increased with the 443 K/15 h aging treatment as shown in Fig. 4 (e).

Fig. 5 (a) presents an EBSD orientation map of EX-II(F) in the ED plane. The associated pole figures, see Fig. 5 (b), indicate a fibrous texture where most of the (10-10) planes were aligned parallel to ED, i. e., the maximum texture intensity was approximately 7. The phase map in Fig. 5 (c) further confirms the existence of granular β eutectic phase. Fig. 5 (d) and (e) show the EBSD orientation maps for the α-matrix and the β eutectic phases, respectively. It is evident that most of the fine-grained β eutectic phase was distributed at the GBs and its average diameter was approximately 0.8 μm in the ED plane.

3.2. Strengthening effect of the β eutectic phase in EX-II(F)

Fig. 6 (a) compares the tensile behavior of AZ80 after different processing conditions. The ultimate tensile strength (R_m) values of the as-cast AZ80 and EX-I(F) were 154 MPa and 388 MPa, respectively. The elongation-to-failure (ε_f) of the EX-I(F) was 16%, which was about three times greater than that of the as-cast AZ80. The R_m and ε_f of EX-II(F) were 425 MPa and 13%, respectively. The R_m of the EX-II(T5) was 440 MPa with the same ε_f (13%). In addition, the yield strength ($R_{p0.2}$) of the EX-II(F) was approximately 288 MPa, which was 68 MPa higher than that for EX-I(F). Fig. 6 (b) presents the microstructure of EX-II(F) in the TD within 2 mm of the tensile fracture. It was composed of the β eutectic phase and the α-Mg matrix. The EDS maps for Mg and Al in Fig. 6 (d, e) are consistent with the phase contrast evident in Fig. 6 (c). Cracks were observed at GBs in the β eutectic phase (indicated by the red arrows in Fig. 6 (b, c)). It is suggested that the α-Mg matrix hinders the crack propagation in the β eutectic phase, which enables higher ε_f values. Consistent with the observations of this work, the β eutectic phase has been shown to provide less plastic deformation and lead to intergranular crack propagation perpendicular to the tensile direction [5]. Four strengthening mechanisms (Equ. (4–7)), including thermal mismatch (TM) [23], Orowan looping (OL) [24], load transfer (LT) [25], and Hall-Petch (HP) [26], have been used to help explain the resulting strengths of the β eutectic phase on the composite-like EX-II(F).

$$\Delta\sigma_{TM} = \alpha G b\left(12\Delta T\Delta C V_p/(b d_p)\right)^{0.5} \tag{4}$$

$$\Delta\sigma_{OL} = \left[MGb\Big/\left(2\pi\sqrt{1-\nu}\right)\right](1/\lambda)\ln(d_p/r),\quad \lambda = 0.5 d_p\left(3\pi/2V_p\right)^{0.5} \tag{5}$$

$$\Delta\sigma_{LT} = \left(V_p\sigma_0\right)/2 \tag{6}$$

$$\Delta\sigma_{HP} = k\left(d_{EX-II(F)}^{-0.5} - d_{EX-I(F)}^{-0.5}\right) \tag{7}$$

where G (1.66×10^4 MPa), b (3.21×10^{-10} m), ν (0.35) are the shear modulus, Burgers vector, and Poisson's ratio, respectively, for the α-Mg matrix [27]. α, M, k are material constants. ΔT is the temperature difference between the extrusion condition and the ambient environment. ΔC is the difference in the average thermal expansion coefficient between the β eutectic phase and the α-matrix [28]. d_p and V_p are the average diameter and volume fraction of the β eutectic phase in the EX-II (F), respectively. r is the inner cut-off radius of the dislocation and is estimated to be equal to b [24]. σ_0 is the yield strength of the unreinforced matrix [29]. $d_{EX-I(F)}$ and $d_{EX-II(F)}$ are the average α-Mg grain sizes

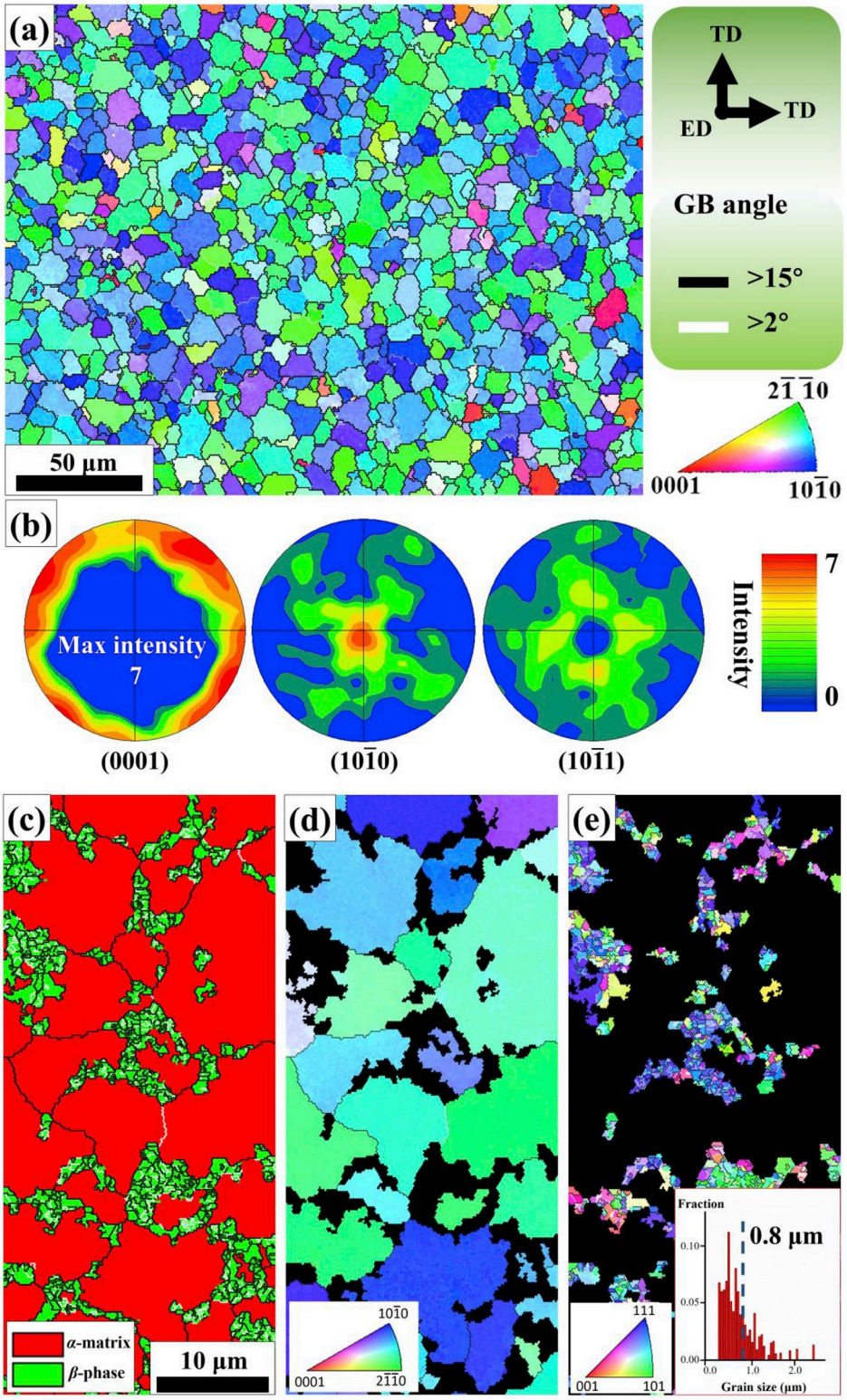

Fig. 5. (a) IPF map for the EX-II(F) in the ED plane, the white and black lines represent the low (2–15°) and high (>15°) angle grain boundaries, respectively; (b) Pole figures in the ED plane; (c) Phase map for the EX-II(F) in the ED plane; IPF maps for the (d) α-Mg matrix and (e) β eutectic phase, the inset in (e) indicates the size distribution of the β grains.

of EX-I(F) and EX-II(F), respectively.

Based on the strengthening mechanisms analysis, the HP, LT, TM, and OL accounted for approximately 33 MPa, 14 MPa, 7 MPa, and 7 MPa of the $R_{p0.2}$ increase compared with EX-I(F), respectively (Table 2). It is noted that shearing of the medium-sized (>100 nm) precipitates by basal slip has been observed in Mg–5Zn [30] and WE43 [31]. Thus, the shearing of the secondary phase (retained β eutectic phase and dynamic precipitates) may additionally strengthen the EX-II(F). Moreover, Jayalakshmi et al. [32] reported that large particles acted as load-bearing members, contributing to increasing the strength, whereas

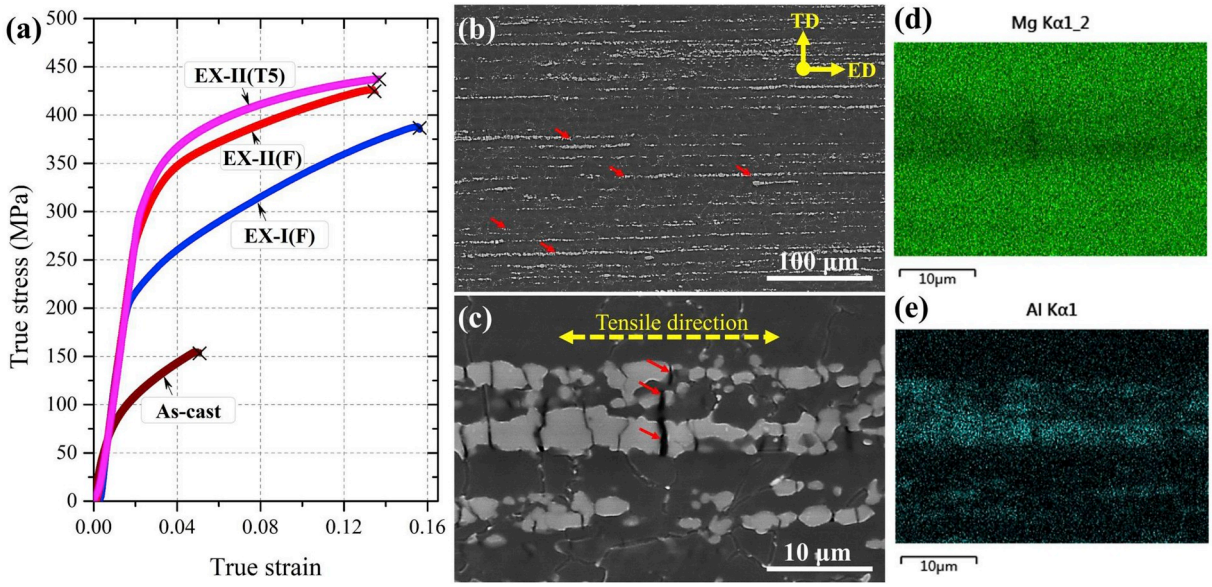

Fig. 6. (a) RT true stress versus true strain curves for AZ80 after different processing conditions; (b) Low-magnification and (c) high-magnification SE-SEM photomicrographs within 2 mm of the RT fracture of EX-II(F) in TD, where the red arrows indicate cracks; (d) and (e) Energy disperse spectroscopy (EDS) maps highlighting the magnesium and aluminum distribution for the area represented in (c). (For interpretation of the references to colour in this figure legend, the reader is referred to the Web version of this article.)

Table 2
Parameters involved in the strengthening mechanism analysis of EX-II(F).

Mechanism	Parameter value	$\Delta\sigma$ (MPa)
Thermal mismatch	$\alpha = 1.25$ $\Delta T = 330$ K, $d_p = 3 \times 10^{-6}$ m, $V_p = 0.13$ $\Delta C = 2 \times 10^{-6}$ m/(m·K)	$\Delta\sigma_{TM} = 7$
Orowan looping	$M = 6.5$, $r \approx b$	$\Delta\sigma_{OL} = 7$
Load transfer	$\sigma_0 = 220$ MPa	$\Delta\sigma_{LT} = 14$
Hall-Petch	$k = 0.28$ MPa m$^{1/2}$, $d_{EX\text{-}I(F)} = 2.6 \times 10^{-5}$ m, $d_{EX\text{-}II(F)} = 1.0 \times 10^{-5}$ m	$\Delta\sigma_{HP} = 33$
Total strengthening	$\Delta\sigma_y = 61$	

the fine second phase particles served more as ε_f enhancers. Thus, the large β eutectic phase (1–3 μm) and fine β precipitates (0.5 μm) can simultaneously increase the R_m and ε_f of EX-II(F). Overall, the EX-II(F) treatment effectively increased the strength while maintaining the ε_f, and this is expected to be due to the following reasons: (i) the high volume percent of β eutectic phase and dynamic precipitates, which favored the fine-grained extruded microstructure and restricted the grain growth during DRX [33]. (ii) The retained β eutectic phase weakened the texture intensity of the EX-II(F), which resulted in a relatively high ε_f value (13%) [34]. (iii) The β eutectic phase was not subjected to the poor hardening effect typically associated with β precipitates, and it pinned dislocation motion both in the GI and near the GBs [24].

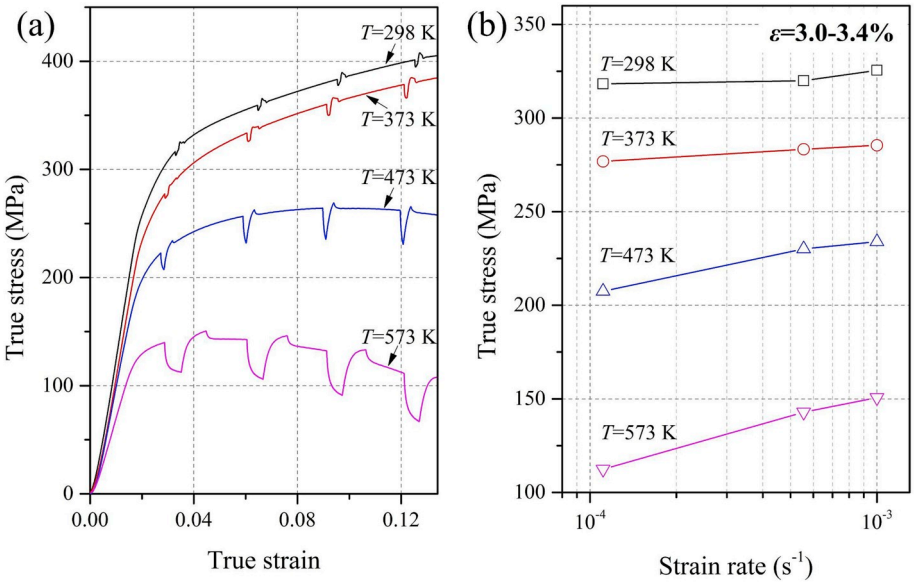

Fig. 7. (a) True stress-true strain curves for the SRJ tests on EX-II(F) at four test temperatures. Each test comprises four SRJs with the strain rates ranging between 10^{-4} s^{-1} to 10^{-3} s^{-1}; (b) Variation of the true stress with the strain rate at 298–573 K and strain levels between 3.0–3.4%.

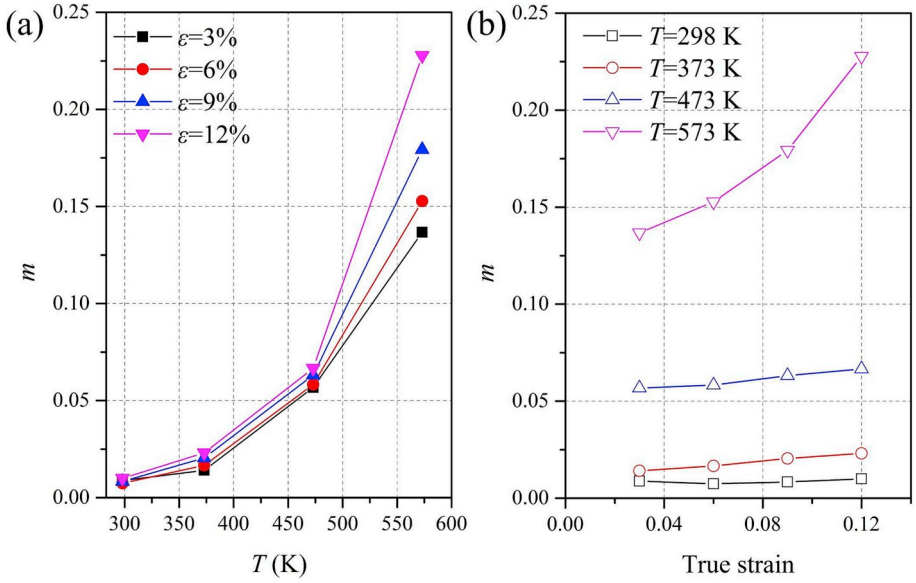

Fig. 8. Variation of SRS exponent, m, as a function of (a) temperature and (b) true strain in EX-II(F).

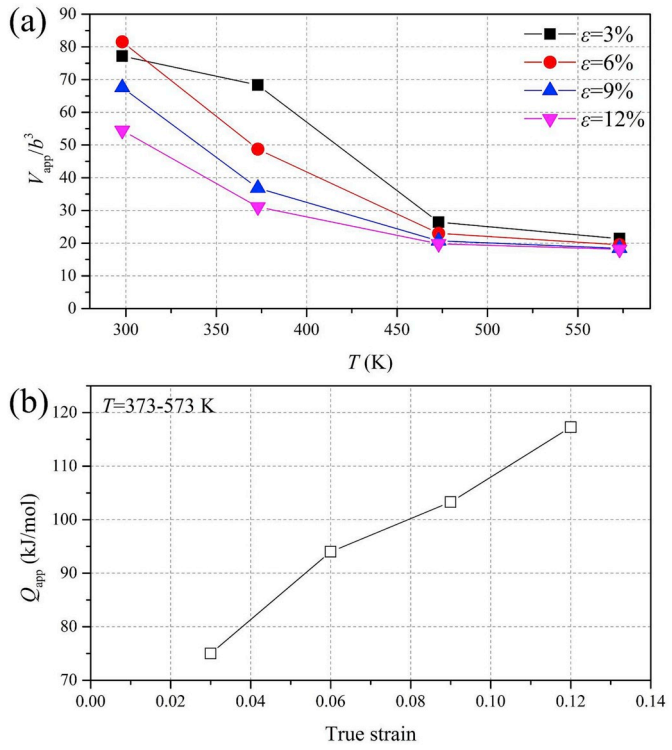

Fig. 9. (a) Variation of the normalized apparent activation volume, V_{app}/b^3, as a function of the temperature at four strain levels in EX-II(F); (b) Apparent activation energy, Q_{app}, at $T = 373$–573 K as a function of the true strain.

3.3. SRS behavior of the EX-II(F) at 298–573 K

The true stress and true strain curves of EX-II(F) are provided as Fig. 7 (a), where four targeted strain levels ($\varepsilon = 3\%$, 6%, 9%, 12%) were selected for the SRJ tests at 298–573 K. Strain hardening was prevalent when T ≤ 373 K, while higher temperatures induced more strain softening and decreased the flow stress, which is expected to be due to the activation of more non-basal slip systems [35]. Fig. 7 (b) shows the variation of flows stress with the strain rate at $\varepsilon = 3.0$–3.4%. Higher temperatures induced a larger fluctuation of the flow stress when the strain rates ranged between 10^{-4}-10^{-3} s^{-1}. At $T = 298$ K, there was only a 7 MPa fluctuation, while a 38 MPa fluctuation was exhibited when $T = 573$ K.

According to Equ. (2), the SRS exponent, m, was calculated at four strain levels and four temperatures. Fig. 8 (a) illustrates that the m-value increased with increasing temperature. At $\varepsilon = 3\%$, the m-value increased from 0.009 to 0.137 when the temperature increased from 298 K to 573 K. The strain level also influenced the m-value, see Fig. 8 (b). The 298 K m-value exhibited less sensitivity to strain. However, with increasing temperature, the m-value had a stronger dependence on the strain level. For example, at $T = 573$ K, the m-value increased from 0.137 to 0.228 when the strain increased from 3% to 12%. Overall, the m-value increased with increasing temperature, which is consistent with Equ. (3). In addition, m was inversely proportional to the apparent activation volume, V_{app}, which decreased with increasing strain. Thus, the higher strain level resulted in larger m-values [36].

The apparent activation volume, V_{app}, and apparent activation energy, Q_{app}, are often correlated to the governing deformation mechanism [35]. Previous literature [18,19,36] reported that face center cubic (FCC) metals exhibit a larger V_{app} (10^2–10^3 b^3) when dislocations are the dominant deformation mechanism. When dislocation glide is suppressed due to decreasing grain size, GB diffusion (with a smaller V_{app}) contributes more to the deformation [18,37]. The V_{app}, provided in Fig. 9 (a) [38], decreased from 80 b^3–20 b^3 with increasing temperature. Higher strain levels also resulted in lower V_{app} values. The Q_{app} of EX-II (F) can be estimated based on the Zener-Hollomon constitutive model [35,39]:

$$\dot{\varepsilon} = A(\sinh(\alpha\sigma))^n \exp\left(-Q_{app}/RT\right) \quad (8)$$

where A and α are the material constants, σ is the flow stress, n is the stress exponent, $\dot{\varepsilon}$ is the strain rate (10^{-4} s^{-1}-10^{-3} s^{-1}), T is the test temperature (373–573 K), and R is the molar gas constant (8.3145 J/(mol·K)). Fig. 9 (b) indicates that the Q_{app} increased from 75 kJ/mol to 120 kJ/mol with increasing strain. The average Q_{app} (~100 kJ/mol) was consistent with previous findings for other Mg alloys [35], which suggests that self-diffusion was involved in the EX-II(F) deformation mechanisms.

3.4. Aging precipitation enhanced SRS behavior

Fig. 10 (a) compares the SRS behavior of both the EX-II(F) and EX-II

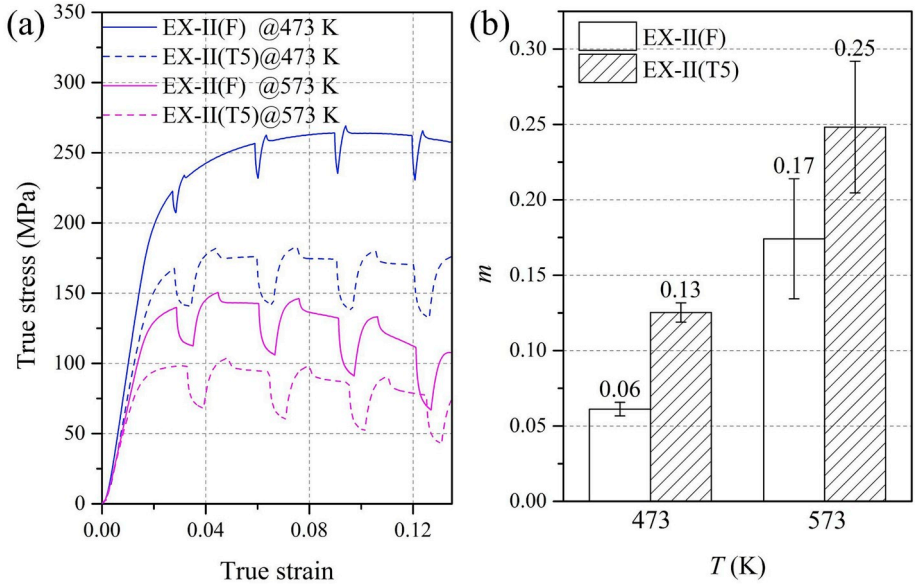

Fig. 10. (a) True stress-true strain curves for the SRJ tests on EX-II(F) and EX-II(T5) at 473 K and 573 K. Each test comprises four SRJs with the strain rates varying from 10^{-4} s^{-1} to 10^{-3} s^{-1}; (b) Average SRS exponent, *m*, as a function of the temperature for the EX-II(F) and EX-II(T5) conditions.

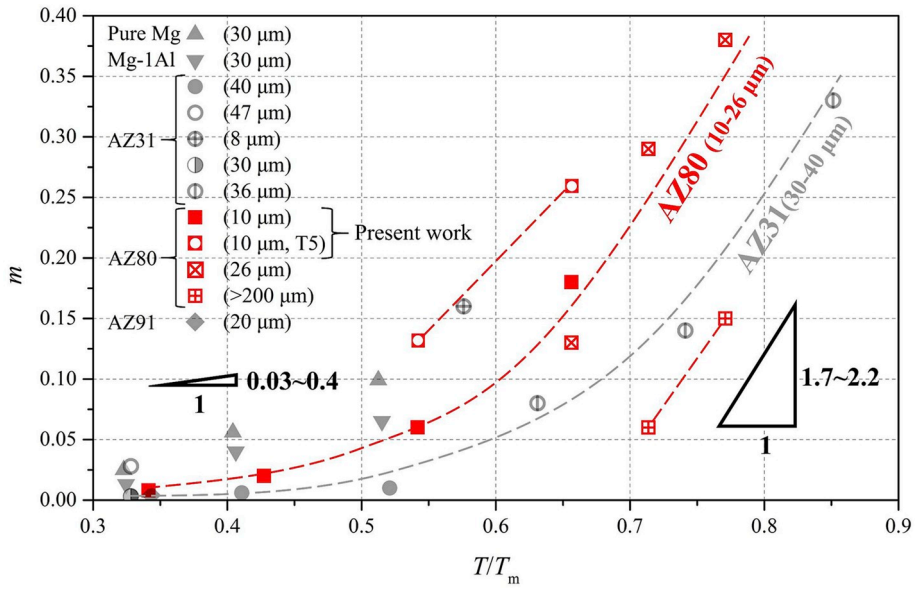

Fig. 11. Variation of *m*-value as a function of temperature, T/T_m, in pure Mg, Mg–1Al, AZ31, AZ80, and AZ91 with different grain sizes. T_m is the melting temperature. All SRS tests were conducted at strain rates which ranged 10^{-6}-10^{-1} s^{-1} [15,17,35,39,40,43–45].

(T5) at 473 K and 573 K. At $T = 473$ K, the flow stress of the EX-II(T5) was approximately 80 MPa lower than that for the F condition. The same trend was observed at 573 K. The β eutectic phase is a brittle phase at RT [5]. However, it exhibited greater deformability and strong softening at $T \geq 573$ K, which resulted in a significant weakening effect for EX-II(T5) [40]. In addition, the Al depletion in the α-Mg phase, resulting from the higher volume percent of the β eutectic phase and β precipitates formed during the T5 treatment, reduces the solute strengthening effect in the α-Mg phase. These factors contributed to the flow stress drop after the T5 treatment. The corresponding average *m* is shown in Fig. 10 (b). The *m*-value increased by 117% and 47% after the T5 treatment at 473 K and 573 K, respectively. The diffusion of the Al solutes to dislocations tends to impede their motion [41], and this solute strengthening effect decreases the *m*-value in Mg alloys [15], however, the the *m*-value remains positive which is often attributed to the hexagonal closed packed crystal structure [42]. As a net result, the Al solute effect tend to result in a lower overall *m*-values. After the aging treatment (e.g., EX-II(T5)), more Al solutes are removed as a result of β precipitation, see Fig. 3 (d). The β precipitates have a primary habit plane parallel to the basal plane of the α-Mg matrix and this result in poor pinning of dislocations [2]. Thus a positive *m*-value is manifested. As a result, the aged specimens exhibit a greater overall *m*-value which is consistent with the result in Fig. 10 (b).

Fig. 11 summarizes the *m*-value variation with temperature in pure Mg and some Mg–Al alloys [15,17,35,39,40,43–45]. Here we define the $\eta = \Delta m/\Delta(T/T_m)$ as a coefficient of the temperature dependence for SRS. The η was 0.03–0.4 when $0.6 > T/T_m > 0.3$ and increased to 1.7–2.2 when $T/T_m > 0.7$. Grain refinement (e.g., AZ31 (8 μm)) and coarsening (e.g., AZ80 (>200 μm)) resulted in higher and lower *m*-values, respectively. Pure Mg and EX-II(T5) exhibited relatively high

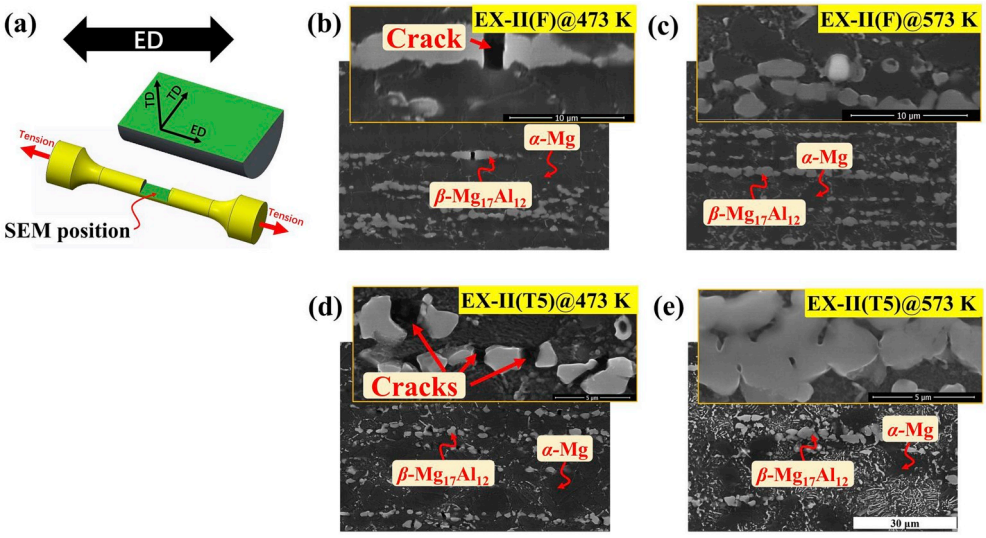

Fig. 12. SE - SEM images for the microstructure of EX-II(F) and EX-II(T5) in the TD plane after SRJ tests at $\varepsilon = 20\%$ for 473 K and 573 K. (a) The schematic map of the observation plane (green) in the tensile specimen; (b, c) Deformed microstructures of EX-II(F) at 473 K and 573 K, respectively; (d, e) Deformed microstructures of EX-II(T5) at 473 K and 573 K, respectively. (For interpretation of the references to colour in this figure legend, the reader is referred to the Web version of this article.)

m values. This further strengthens the argument for the increasing *m*-value trend with decreasing Al solute concentration. The synergistic effect of the Al solute concentration and grain size is presented in Fig. 11. Although the Al solute concentration of AZ31 is lower than that for AZ80, the larger grain size for AZ31 (30–40 μm) resulted in a lower *m*-value than for AZ80, which exhibited a 10–26 μm grain size.

The microstructures after SRJ deformation ($\varepsilon = 20\%$) at 473 K and 573 K in EX-II(F) and EX-II(T5) were characterized, see Fig. 12. β eutectic phase cracking was prevalent at 473 K and became more frequent at lower temperatures, which is consistent with previous findings [5]. There was little occurrence of β eutectic phase cracking when the deformation temperature increased to 573 K. This was attributed to the high deformability of the β eutectic phase above 573 K [40].

4. Summary and conclusions

AZ80 was processed using extrusion without a homogenization pretreatment (EX-II(F)) and with a homogenization pretreatment (EX-I(F)). The microstructure and tensile properties were investigated in EX-II(F) and EX-II(T5), which represents the aging condition after the extrusion, and the β-eutectic-phase strengthening mechanisms on the yield strength were analyzed. In addition, the temperature and strain dependence for SRS were investigated, and the influence of aging on the SRS behavior was discussed. The following conclusions were offered:

(1) The 13 vol% fine-grained β eutectic phase particles and dynamic precipitates contributed to basal texture weakening and DRX grain refinement (~10 μm) in the EX-II(F). The β eutectic phase was stable during the 443 K/15 h aging treatment (EX-II(T5)).

(2) The EX-II(F) exhibited $R_m = 425$ MPa, $R_{p0.2} = 288$ MPa, and an $\varepsilon_f = 13\%$. Four strengthening mechanisms, including the Hall-Petch, load transfer, thermal mismatch, and Orowan looping, were suggested to account for approximately 33 MPa, 14 MPa, 7 MPa, and 7 MPa of the $R_{p0.2}$ increase compared to that of EX-I(F), respectively.

(3) The *m*-value increased from 0.009 to 0.137 when the temperature increased from 298 K to 573 K in EX-II(F). Higher temperatures induced a faster increase of the *m*-value with increasing strain. The V_{app} and the average Q_{app} were 20–70 b^3 and 100 kJ/mol, respectively, for EX-II(F) at 373–573 K, which implied that self-diffusion played a role in the deformation mechanisms.

(4) Aging precipitation decreased the flow stress of EX-II(F) at 473–573 K. The *m*-value of the EX-II(T5) was 117% and 47% larger than that of EX-II(F) at 473 K and 573 K, respectively. This was explained by the decreased Al solute in the Mg matrix phase at higher temperatures and after the aging treatment. β eutectic phase cracking decreased with increasing temperature, which was attributed to the higher deformability of the β eutectic phase above 573 K.

Data availability statement

The raw data required to reproduce these findings cannot be shared at this time as the data also forms part of an ongoing study.

Acknowledgments

This work was financially supported by the China Scholarship Council (201707000086). Acknowledgments are given to the 2015 Cultivation Program for the Excellent Doctoral Dissertation of Southwest Jiaotong University (received by Lingbao Ren), the Program of the 2015 Doctoral Innovation Fund of Southwest Jiaotong University (received by Lingbao Ren), and the support from Litmat Technology Chengdu Co., Ltd. The authors also acknowledge the technical support of Dr. Askeland Per and Mr. David Hernández Escobar of Michigan State University.

References

[1] S. Barbagallo, H.I. Laukli, O. Lohne, E. Cerri, Divorced eutectic in a HPDC magnesium-aluminum alloy, J. Alloy. Comp. 378 (2004) 226–232.
[2] J.F. Nie, Precipitation and hardening in magnesium alloys, Metall. Mater. Trans. A 43 (2012) 3891–3939.
[3] P. Schobinger-Papamantellos, P. Fischer, Neutronenbeugungsuntersuchung der Atomverteilung von $Mg_{17}Al_{12}$, Naturwissenschaften 57 (1970) 128–129.
[4] Z.W. Huang, Y.H. Zhao, H. Hou, P.D. Han, Electronic structural, elastic properties and thermodynamics of $Mg_{17}Al_{12}$, Mg_2Si and Al_2Y phases from first-principles calculations, Phys. B Condens. Matter 407 (2012) 1075–1081.
[5] H. Zhang, S.L. Shang, Y. Wang, A. Saengdeejing, L.Q. Chen, Z.K. Liu, First-principles calculations of the elastic, phonon and thermodynamic properties of $Al_{12}Mg_{17}$, Acta Mater. 58 (2010) 4012–4018.
[6] S. Celotto, TEM study of continuous precipitation in Mg-9 wt%Al-1 wt%Zn alloy, Acta Mater. 48 (2000) 1775–1787.
[7] P. Donnadieu, S. Benrhaiem, C. Tassin, F. Volpi, J.J. Blandin, Preparation, microstructure and properties of magnesium-γ$Mg_{17}Al_{12}$ complex metallic alloy in situ composites, J. Alloy. Comp. 702 (2017) 626–635.

[8] M. Zha, H.M. Zhang, C. Wang, H.Y. Wang, E.B. Zhang, Q.C. Jiang, Prominent role of a high volume fraction of $Mg_{17}Al_{12}$ particles on tensile behaviors of rolled Mg-Al-Zn alloys, J. Alloy. Comp. 728 (2017) 682–693.
[9] J.M. Wheeler, V. Maier, K. Durst, M. Göken, J. Michler, Activation parameters for deformation of ultrafine-grained aluminium as determined by indentation strain rate jumps at elevated temperature, Mater. Sci. Eng. A 585 (2013) 108–113.
[10] P. Wu, D. Tang, M.J. Worswick, H. Wang, Y. Peng, S. Kurukuri, D. Li, Strain rate sensitivities of deformation mechanisms in magnesium alloys, Int. J. Plast. 107 (2018) 207–222.
[11] J.A. del Valle, O.A. Ruano, Influence of the grain size on the strain rate sensitivity in an Mg-Al-Zn alloy at moderate temperatures, Scr. Mater. 55 (2006) 775–778.
[12] Q. Yang, A.K. Ghosh, Deformation behavior of ultrafine-grain (UFG) AZ31B Mg alloy at room temperature, Acta Mater. 54 (2006) 5159–5170.
[13] N. Bayat Tork, S.H. Razavi, H. Saghafian, R. Mahmudi, Strain-rate sensitivity of Mg-Gd alloys after extrusion and simple shear extrusion, Mater. Sci. Technol. 33 (2017) 2244–2252.
[14] G.C. Wang, M.W. Fu, Maximum m superplasticity deformation for Ti-6Al-4V titanium alloy, J. Mater. Process. Technol. 192–193 (2007) 555–560.
[15] H.Q. Ang, S. Zhu, T.B. Abbott, D. Qiu, M.A. Easton, Strain-rate sensitivity of die-cast magnesium-aluminium based alloys, Mater. Sci. Eng. A 699 (2017) 239–246.
[16] L. Jiang, J.J. Jonas, R.K. Mishra, A.A. Luo, A.K. Sachdev, S. Godet, Twinning and texture development in two Mg alloys subjected to loading along three different strain paths, Acta Mater. 55 (2007) 3899–3910.
[17] Y.B. Chun, C.H.J. Davies, Twinning-induced negative strain rate sensitivity in wrought Mg alloy AZ31, Mater. Sci. Eng. A 528 (2011) 5713–5722.
[18] L. Lu, R. Schwaiger, Z.W. Shan, M. Dao, K. Lu, S. Suresh, Nano-sized twins induce high rate sensitivity of flow stress in pure copper, Acta Mater. 53 (2005) 2169–2179.
[19] G. Mohanty, J.M. Wheeler, R. Raghavan, J. Wehrs, M. Hasegawa, S. Mischler, L. Philippe, J. Michler, Elevated temperature, strain rate jump microcompression of nanocrystalline nickel, Philos. Mag. 95 (2015) 1878–1895.
[20] L.B. Ren, G.F. Quan, C.J. Boehlert, M.Y. Zhou, Y.Y. Guo, L.L. Fan, The microstructure evolution and deformation behavior of AZ80 during gradient increment cyclic loading, Metall. Mater. Trans. A 49 (2018) 3692–3702.
[21] J.C. Tan, M.J. Tan, Dynamic continuous recrystallization characteristics in two stage deformation of Mg-3Al-1Zn alloy sheet, Mater. Sci. Eng. A 339 (2003) 124–132.
[22] E.A. Mørtsell, S.J. Andersen, J. Friis, C.D. Marioara, R. Holmestad, Atomistic details of precipitates in lean Al-Mg-Si alloys with trace additions of Ag and Ge studied by HAADF-STEM and DFT, Philos. Mag. 97 (2017) 851–866.
[23] W.S. Miller, F.J. Humphreys, Strengthening mechanisms in particulate metal matrix composites, Scr. Metall. Mater. 25 (1991) 33–38.
[24] C.R. Hutchinson, J.F. Nie, S. Gorsse, Modeling the precipitation processes and strengthening mechanisms in a Mg-Al-(Zn) AZ91 alloy, Metall. Mater. Trans. A 36 (2005) 2093–2105.
[25] V.C. Nardone, K.M. Prewo, On the strength of discontinuous silicon carbide reinforced aluminum composites, Scr. Metall. 20 (1986) 43–48.
[26] A.F. Crawley, K.S. Milliken, Precipitate morphology and orientation relationships in an aged Mg-9% Al-1% Zn-0.3% Mn alloy, Acta Metall. 22 (1974) 557–562.
[27] W.J. Kim, I.B. Park, S.H. Han, Formation of a nanocomposite-like microstructure in Mg-6Al-1Zn alloy, Scr. Mater. 66 (2012) 590–593.
[28] P.D. Pathak, R.J. Desai, Thermal expansion of magnesium and temperature variation of negative second moment of its frequency spectrum, Phys. Status Solidi A 66 (1981) K179–K182.
[29] M. Mabuchi, K. Higashi, Strengthening mechanisms of Mg-Si alloys, Acta Mater. 44 (1996) 4611–4618.
[30] J.T. Wang, N. Stanford, Investigation of precipitate hardening of slip and twinning in Mg5%Zn by micropillar compression, Acta Mater. 100 (2015) 53–63.
[31] J.J. Bhattacharyya, F. Wang, N. Stanford, S.R. Agnew, Slip mode dependency of dislocation shearing and looping of precipitates in Mg alloy WE43, Acta Mater. 146 (2018) 55–62.
[32] S. Jayalakshmi, S. Sankaranarayanan, S.P.X. Koh, M. Gupta, Effect of Ag and Cu trace additions on the microstructural evolution and mechanical properties of Mg–5Sn alloy, J. Alloy. Comp. 565 (2013) 56–65.
[33] K.K. Deng, X.J. Wang, Y.W. Wu, X.S. Hu, K. Wu, W.M. Gan, Effect of particle size on microstructure and mechanical properties of SiCp/AZ91 magnesium matrix composite, Mater. Sci. Eng. A 543 (2012) 158–163.
[34] R.K. Sabat, R.K. Mishra, A.K. Sachdev, S. Suwas, The deciding role of texture on ductility in a Ce containing Mg alloy, Mater. Lett. 153 (2015) 158–161.
[35] L.B. Ren, J. Wu, G.F. Quan, Plastic behavior of AZ80 alloy during low strain rate tension at elevated temperature, Mater. Sci. Eng. A 612 (2014) 278–286.
[36] M.A. Meyers, A. Mishra, D.J. Benson, Mechanical properties of nanocrystalline materials, Prog. Mater. Sci. 51 (2006) 427–556.
[37] Q. Wei, S. Cheng, K.T. Ramesh, E. Ma, Effect of nanocrystalline and ultrafine grain sizes on the strain rate sensitivity and activation volume: fcc versus bcc metals, Mater. Sci. Eng. A 381 (2004) 71–79.
[38] M.F. Ashby, H.J. Frost, Deformation-mechanism Maps, Pergamon Press., London, 1982.
[39] L.B. Ren, M.Y. Zhou, Y.W.X. Zhang, C.J. Boehlert, G.F. Quan, Effect of 0.4 wt% yttrium addition and heat treatment on the high-temperature compression behavior of cast AZ80, J. Mater. Sci. 54 (2019) 5757–5772.
[40] J. Ragani, P. Donnadieu, C. Tassin, J.J. Blandin, High-temperature deformation of the γ-$Mg_{17}Al_{12}$ complex metallic alloy, Scr. Mater. 65 (2011) 253–256.
[41] L. Jiang, J.J. Jonas, R. Mishra, Effect of dynamic strain aging on the appearance of the rare earth texture component in magnesium alloys, Mater. Sci. Eng. A 528 (2011) 6596–6605.
[42] M.A. Meyers, Dynamic Behaviour of Materials, John Wiley & Sons, New York, 1994.
[43] C.H.J. Davies, The effect of twinning on strain rate sensitivity during the compression of extruded magnesium alloy AZ31, Mater. Sci. Forum 539–543 (2007) 1723–1728.
[44] E. Karimi, A. Zarei-Hanzaki, M.H. Pishbin, H.R. Abedi, P. Changizian, Instantaneous strain rate sensitivity of wrought AZ31 magnesium alloy, Mater. Des. 49 (2013) 173–180.
[45] N. Stanford, I. Sabirov, G. Sha, A. La Fontaine, S.P. Ringer, M.R. Barnett, Effect of Al and Gd solutes on the strain rate sensitivity of magnesium alloys, Metall. Mater. Trans. A Phys. Metall. Mater. Sci. 41 (2010) 734–743.